Colloids and Surfaces B: Biointerfaces 214 (2022) 112455

Contents lists available at ScienceDirect

Colloids and Surfaces B: Biointerfaces

journal homepage: www.elsevier.com/locate/colsurfb

Electroactive calcium-alginate/polycaprolactone/reduced graphene oxide nanohybrid hydrogels for skeletal muscle tissue engineering

J.L. Aparicio-Collado [a], N. García-San-Martín [a], J. Molina-Mateo [a], C. Torregrosa Cabanilles [a], V. Donderis Quiles [b], A. Serrano-Aroca [c,*], R. Sabater i Serra [a,b,d,**]

[a] Centre for Biomaterials and Tissue Engineering, Universitat Politècnica de València, Spain
[b] Department of Electrical Engineering, Universitat Politècnica de València, Spain
[c] Biomaterials and Bioengineering Lab, Centro de Investigación Traslacional San Alberto Magno, Universidad Católica de Valencia San Vicente Mártir, Valencia, Spain
[d] Biomedical Research Networking Centre in Bioingenieering, Biomaterials and Nanomedicine (CIBER-BBN), Spain

ARTICLE INFO

Keywords:
Reduced graphene oxide
Nanohybrid hydrogel
Myoblast differentiation
Alginate
Semi-interpenetrated networks

ABSTRACT

Graphene derivatives such as reduced graphene oxide (rGO) are used as components of novel biomaterials for their unique electrical properties. Electrical conductivity is a crucial factor for muscle cells, which are electrically active. This study reports the development of a new type of semi-interpenetrated polymer network based on two biodegradable FDA-approved biomaterials, sodium alginate (SA) and polycaprolactone (PCL), with Ca^{2+} ions as SA crosslinker. Several drawbacks such as the low cell adhesion of SA and weak structural stability can be improved with the incorporation of PCL. Furthermore, this study demonstrates how this semi-IPN can be engineered with rGO nanosheets (0.5% and 2% wt/wt rGO nanosheets) to produce electroactive nanohybrid composite biomaterials. The study focuses on the microstructure and the enhancement of physical and biological properties of these advanced materials, including water sorption, surface wettability, thermal behavior and thermal degradation, mechanical properties, electrical conductivity, cell adhesion and myogenic differentiation. The results suggest the formation of a complex nano-network with different interactions between the components: bonds between SA chains induced by Ca^{2+} ions (*egg-box* model), links between rGO nanosheets and SA chains as well as between rGO nanosheets themselves through Ca^{2+} ions, and strong hydrogen bonding between rGO nanosheets and SA chains. The incorporation of rGO significantly increases the electrical conductivity of the nanohybrid hydrogels, with values in the range of muscle tissue. *In vitro* cultures with C2C12 murine myoblasts revealed that the conductive nanohybrid hydrogels are not cytotoxic and can greatly enhance myoblast adhesion and myogenic differentiation. These results indicate that these novel electroactive nanohybrid hydrogels have great potential for biomedical applications related to the regeneration of electroactive tissues, particularly in skeletal muscle tissue engineering.

1. Introduction

Alginate-based hydrogels are usually produced by crosslinking alginate polymer chains with divalent cations such as Ca^{2+} [1]. Although alginate-based hydrogels possess excellent properties for a broad range of industrial applications [2,3], Ca^{2+} ionically cross-linked alginate hydrogels possess weak mechanical properties within a few hours in physiological solution or immersed in distilled water at body temperature (37°C) [4]. In addition, the hydrophilic nature of alginate hydrogels leads to a lack of cell adhesion [5,6]. Several reinforcing strategies can be used to overcome these issues such as incorporating a hydrophobic polymer with good mechanical properties in the form of semi-interpenetrated polymer networks (semi-IPNs), in which only the hydrophilic polymer networks are crosslinked [7] and/or incorporating carbon nanomaterials (CBNs) [4,8]. Among hydrophobic polymers, the synthetic and biodegradable polymer polycaprolactone (PCL) has good mechanical performance and have shown great potential in biomedical applications such as tissue engineering and drug delivery [9,10]. PCL possesses low melting temperature and superior viscoelastic performance, which render it easy to process into a broad range of shapes and

* Corresponding author at: Biomaterials and Bioengineering Lab, Universidad Católica de Valencia San Vicente Mártir, Spain.
** Corresponding author at: Centre for Biomaterials and Tissue Engineering, Universitat Politècnica de València, Spain.
E-mail addresses: angel.serrano@ucv.es (A. Serrano-Aroca), rsabater@die.upv.es (R. Sabater i Serra).

https://doi.org/10.1016/j.colsurfb.2022.112455
Received 1 February 2022; Received in revised form 6 March 2022; Accepted 8 March 2022
Available online 11 March 2022

sizes [11]. Furthermore, alginate and PCL are Food and Drug Administration-approved materials for biomedical applications [12,13]. Previous studies found that CBNs combined with natural or synthetic polymers can reinforce the biomaterials' mechanical properties, enhance cell adhesion, proliferation [14] and differentiation into several lineages [15], such as osteo-, neural- [16] or skeletal muscle [17].

Graphene (G), one of the most promising CBNs is a two-dimensional material forming a lattice with unique properties [18]. The family of G related materials includes graphene oxide (GO), and reduced graphene oxide (rGO), obtained after GO reduction [16]. Graphene-based composites have been suggested as promising novel biomaterials in the field of regenerative medicine [19], particularly in skeletal muscle regeneration [20–23]. Composites based on natural polymers, such as gelatin with graphene oxide (GO) nanosheets [24] and aligned polysaccharides with graphene fibers [25], have been shown to promote spontaneous differentiation of C2C12 myoblasts. Shin et al. [26] fabricated hybrid fibers matrices composed of poly(lactic-co-glycolic acid)-Collagen impregnated with GO which stimulated cell attachment and myogenic differentiation of murine myoblast cultured in growth medium; moreover, myogenesis was further enhanced using differentiation medium.

Among the properties of G and rGO nanomaterials, its exceptional conductivity stands out [27,28], which make them useful for producing conductive polymer-based composites [29–31]. Although rGO sheets have certain structural defects, lower conductivity and mechanical strength than pristine G sheets, their lower cost and excellent scalable synthesis has enabled many advanced nanocomposites containing rGO to be developed with excellent physical properties [32]. Electrical conductivity is essential for muscle cells, just as it is for neural and cardiac cells. It has been postulated that electrically conductive cell environments could, by themselves, facilitate electrical communication between muscle cells, thus stimulating myogenesis [15]. Composites based on rGO and polyacrylamide (PAAm) enhanced myogenic differentiation compared with GO/PAAm [33], however, it has also been reported that cell response can be conditioned by the reduction method employed to obtain rGO [15].

In this study, we have prepared novel nanohybrid hydrogels based on sodium alginate and polycaprolactone (SA/PCL semi-IPN with Ca^{2+} ions as alginate crosslinker) with incorporated conductive rGO nanosheets with the aim to overcome the drawback of alginate hydrogels (weak structural stability in aqueous environments and poor cell adhesion) and stimulate bioactivity. The incorporated rGO nanosheets will provide bioactivity (in the form of intrinsic electrical conductivity) suitable for the regeneration of electroactive tissues, such as skeletal muscle, cardiac and neural tissue. We hypothesize that the combination of alginate and a very small amount of PCL (10% *wt/wt*) in the form of semi-IPN with embedded rGO nanoparticles (0.5 or 2% with respect to the total mass of polymers) could produce highly stable conductive nanohybrid hydrogels with enhanced physical and biological properties with promising prospects for skeletal muscle tissue engineering. This percentage (10% of PCL) was chosen to keep the hydrophilic properties of calcium alginate, while enhancing its mechanical and cell adhesion properties. Since carbon-based materials, such as rGO, are still quite expensive materials, low percentages of rGO were also selected to reduce production costs as much as possible and avoid potential biocompatibility issues. The physico-chemical properties of the nanohybrid composites were characterized by field emission scanning electron microscopy (HRFESEM), atomic force microscopy (AFM), Fourier transformed infrared spectroscopy (FTIR), water sorption, surface wettability, differential scanning calorimetry (DSC), thermogravimetry (TGA), dynamic mechanical thermal analysis (DMTA) and impedance analysis (electrical conductivity). Furthermore, the biological behavior of C2C12 skeletal myoblast cultures in the nanohybrid hydrogels were analysed to explore their biocompatibility and bioactivity (in terms of cell adhesion and myogenic differentiation).

2. Materials and methods

2.1. Materials

Polyaprolactone (PCL) (molecular weight 43–50 kDa, Product Code 19561) was purchased from Polysciences. Sodium Alginate from brown algae (SA) (538 kDa, ~250 cP, M/G ratio: 0.85, product code 71238) was supplied by Merck. Dioxane and anhydrous calcium chloride ($CaCl_2$) were provided by Scharlab. Reduced graphene oxide (product code C459/rGOB070) was purchased from Graphenea (Spain). Water was purified with a MiliQ Direct Q 3, 5, 8 system from Millipore. All reagents were used as received.

2.2. Fabrication of crosslinked SA and semi-IPN SA/PCL 90/10

SA was dissolved in ultrapure water (Mili-Q) (2% *wt/wt*) at room temperature with constant stirring overnight. PCL was dissolved in dioxane (1% *wt/wt*), also with constant stirring for 2 h at room temperature. To obtain the SA/PCL blends, SA and PCL solutions were mixed with magnetic stirring for 24 h at 85 ºC with a 90/10 *wt/wt* ratio. SA/PCL 90/10 blend films were obtained after the solvent evaporation in an air oven at 50 ºC for 72 h. Reference samples (pristine SA and PCL) were obtained from the initial polymer solutions poured into Petri dishes. Pristine SA films were kept at 50 ºC in an air oven and PCL films were placed at room temperature until solvent evaporation (72 h in both cases).

SA and SA/PCL 90/10 blend films were ionically crosslinked by immersion in a 2% *wt/wt* $CaCl_2$ solution for 2 h (sodium alginate turns into calcium alginate after crosslinking). After that, the films were rinsed three times in Mili-Q water to remove any salt residue, left 48 h at room temperature to evaporate water and dried at 50 ºC under vacuum until constant weight to remove traces of moisture.

2.3. Production of electroactive SA/PCL semi-IPN with embedded rGO nanosheets

The semi-IPNs with incorporated rGO nanosheets were prepared following the same procedure described in Section 2.2 but including an additional previous step. Two different concentrations of rGO (0,5% *wt/wt* and 2% *wt/wt* of the total polymeric weight) were first dispersed (ultrasonic bath for 6 h) in the specific amount of MiliQ water needed to dissolve SA to obtain a homogeneous dispersion of the nanoparticles and avoid aggregates. Then, the nanohybrid composites were obtained following the same procedure described previously.

The scheme with the different steps followed to prepare the semi-IPN and the nanohybrid hydrogels is shown in Fig. 1a, and the notation and sample compositions are indicated in Table 1.

2.4. Characterization techniques

2.4.1. Electron microscopy

The morphology of the samples was analysed by HRFESEM (GeminiSEM 500, Carl Zeiss Microscopy) with an accelerating voltage of 0.8–1.0 kV. The samples were coated with a platinum layer (EM MED020, Leica). Samples were previously hydrated until equilibrium and then freeze-dried to preserve the porous structure. The cross-section was observed after cryogenic fracture.

2.4.2. Atomic force microscopy

The surface topography of the semi-IPN SA/PCL-E and the nanohybrid hydrogel with 2% of rGO nanosheets was analysed by AFM (NanoScope IIIa, Veeco) operating in tapping mode in air (75 kHz resonance frequency and 2.8 N/m constant force). Drive amplitude (600 mV), amplitude set point Asp (1.8 V) and A∞ /A0 (0.8) were set. Nanoscope 5.30r2 software was used for image processing. Roughness of samples was measured from AFM images (300 nm × 300 nm). Root-

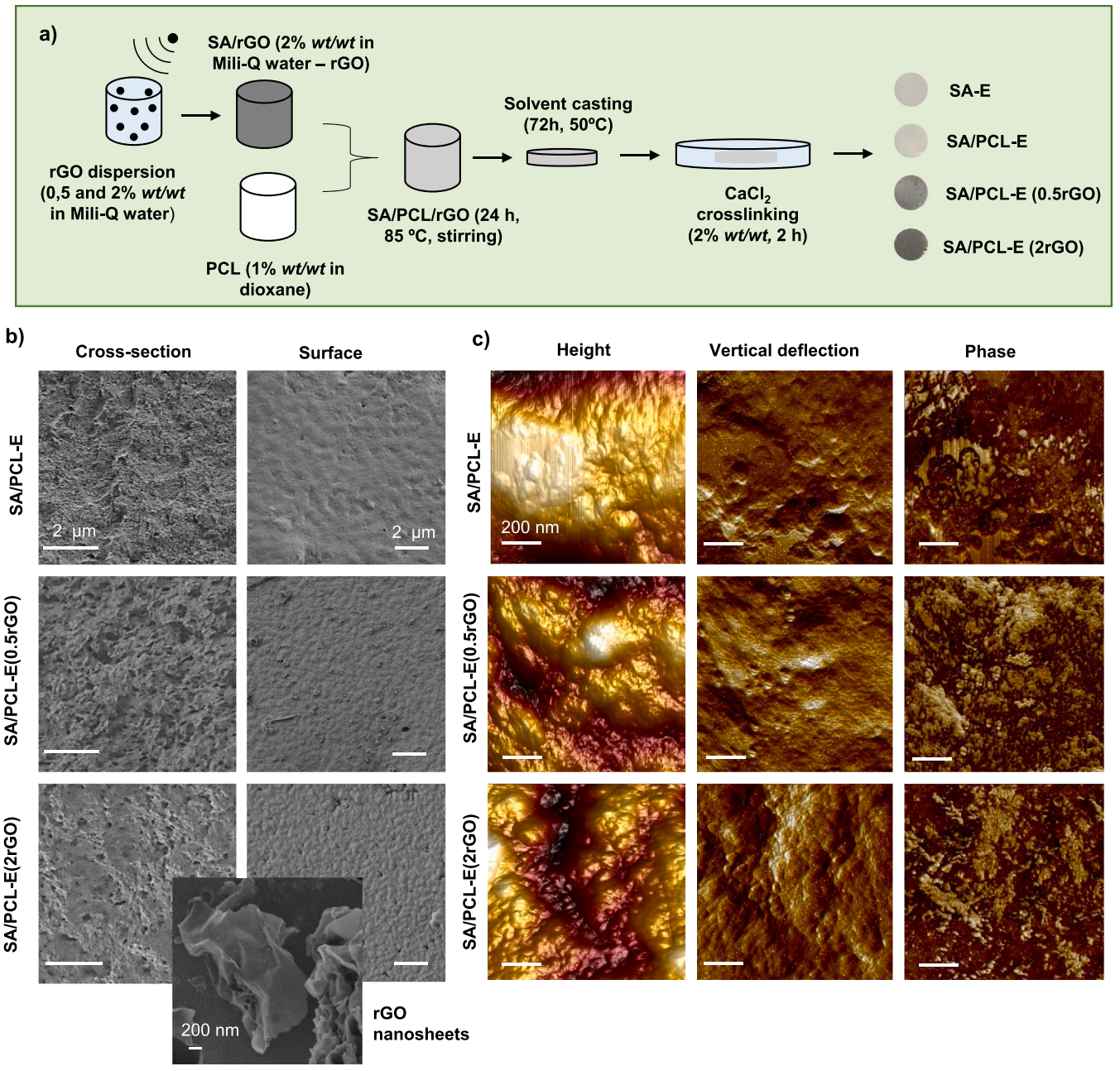

Fig. 1. (a) Scheme with the steps followed to prepare the semi-IPN and the nanohybrid hydrogels. (b) High-resolution field-emission scanning electron microscopy (HRFSEM) images of the cross-section (left column) and surface (right column) in freeze-dried samples. The image at the bottom shows pristine rGO nanosheets dispersed previously in water. (c) Representative Atomic Force microscopy (AFM) images (height, vertical deflection, and phase) of the semi-IPN SA/PCL-E and nanohybrid hydrogels with 0.5% and 2% of rGO.

Table 1
Sample notation and composition.

Sample	Sample description (composition)
PCL	100% Polycaprolactone
SA	100% Sodium alginate
SA-E	100% crosslinked SA
SA/PCL	Blend 90% SA/10% PCL
SA/PCL-E	Semi-IPN (90% SA/10% PCL)
SA/PCL-E(0.5rGO)	Semi-IPN nanohybrid hydrogel SA/PCL 90/10 + 0.5% rGO nanosheets
SA/PCL-E(2rGO)	Semi-IPN nanohybrid hydrogel SA/PCL 90/10 + 2% rGO nanosheets

mean-square average of height deviations taken from the mean image data plane (R_q) was calculated using the roughness subroutine of Nanoscope software.

2.4.3. Fourier transformed infrared spectroscopy (FTIR)

The presence of specific (chemical) groups was determined by FTIR spectroscopy (Bruker Optics FTIR Alpha II). FTIR spectra were collected in transmittance mode from 4000 to 400 cm^{-1} after 24 scans at a resolution of 2 cm^{-1}.

2.4.4. Swelling assay

Swelling experiments were performed in crosslinked samples. Circular samples (ca. 3,8 cm^2) were vacuum-dried at 60 ºC and subsequently immersed in Mili-Q water at 37 ºC for 24 h until equilibrium. Experiments were performed in triplicate.

Samples were weighed before (W_0) and after (W_1) swelling. The swelling degree (W_{eq}) was calculated as follows:

$$W_{eq}(\%) = \frac{W_1 - W_0}{W_0} \cdot 100 \quad (1)$$

2.4.5. Surface wettability

Surface wettability was determined by water contact angle (WCA) using the sessile drop method. A Mili-Q water drop (3 μL) was deposited gravimetrically onto the surface to measure the contact angle and stabilization was allowed (~5 s). WCA was measured by an optical contact angle and contour analysis system (Dataphysics OCA 20). All measurements were performed in quintuplicate to ensure reproducibility.

2.4.6. Differential scanning calorimetry (DSC)

DSC analysis was carried out by a PerkinElmer DSC 8000 under a flowing nitrogen atmosphere (20 mL/min). Samples were subjected to a single heating scan from − 80–240 ºC at 20 ºC/min.

2.4.7. Thermogravimetric analysis (TGA)

Thermal stability and decomposition were analysed by a thermogravimetric analyser Mettler Toledo TGA 2 (SF) system. Vacuum-dried samples (5–10 mg weight) were heated from 30 to 600ºC at a rate of 30ºC/min. The mass of the samples was constantly measured as a function of temperature.

2.4.8. Mechanical properties (DMTA)

Dynamic mechanical thermal analysis (DMTA) was performed with a Perking Elmer DMA 8000 at a frequency of 1 Hz on sample bars (20 × 5 × 0.01 mm) in an immersion bath (Mili-Q water). The storage modulus (E') and loss modulus (E'') was measured in the temperature range 35–39 ºC at a heating rate of 1 ºC/min.

2.4.9. Electrical properties

Electrical characterization was performed by the Agilent 16451B parallel plates (circular electrodes 5 mm in diameter) connected to an impedance analyser Hewlett Packard 4284 A LCR Meter. Complex impedance was obtained at frequencies 20, 50 and 100 kHz at room temperature. Electrical conductivity (σ) was calculated (S/m) as:

$$\sigma = \frac{l}{R_S \cdot A} \quad (2)$$

Where l is the sample thickness, R_s is the real part of the complex impedance and A is the electrode area. The measurements were performed in triplicate.

2.5. Cell culture and biological characterization

Murine myoblasts (C2C12, Sigma Aldrich; Merck) were cultured in high glucose Dulbeco's Modified Eagle's Medium (DMEM, Biowest) supplemented with 10% fetal bovine serum (FBS, ThermoFisher) and 1% Penicillin/Streptomycin (P/S, ThermoFisher) in a humidified atmosphere at 37 ºC and 5% CO_2. Cells were passed during amplification at maximum 80% confluence.

2.5.1. Cytotoxicity

Cytotoxicity was performed by adapting the ISO/EN10993 standard to evaluate in vitro toxicity from the extracts (indirect method) by mean of an MTT (3-[4, 5-dimethylthiazol-2-yl]−2, 5 diphenyl tetrazolium bromide) assay. The ratio of material surface to extraction fluid was 2.5 cm^2/mL (sample thickness ca. 200 μm). 96-well plates were seeded with 10^4 cells/well with 100 μL of growth medium (DMEM + 10% FBS + 1% P/S) and placed in the incubator. At the same time, autoclaved crosslinked samples (121 ºC, 20 min) were cultured overnight in growth medium to generate the extracts. After 24 h of culture, the medium was replaced by 100 μL of the extracts. Culture medium (growth medium) was used as negative control (life) and natural rubber latex extract was the positive control (death). Each sample was studied with three biological replicates.

After 24, 48 and 72 h, supernatant was replaced by 100 μL of new growth medium without phenol red containing a 1:10 MTT dilution (Sigma Aldrich; Merck). Viable cells were stained with water-insoluble formazan dye. After incubation for 4 h, the solution was removed and 100 μL of solubilization buffer (10% SDS in 0.01 M HCl) (Sigma Aldrich; Merck) was added to each well and left overnight at 37 ºC to dissolve the formazan crystals. Optical density was then measured by a microplate reader (Victor Multilabel Plate Reader, Perkin Elmer) at 570 nm wavelength. Cell viability was calculated as:

$$Viability \quad (\%) = \frac{OD \quad test}{OD \quad control} \cdot 100 \quad (3)$$

where *OD test* is the optical density of the sample and *OD control* is the optical density of the negative control.

2.5.2. Cell adhesion

Cell adhesion was studied by fluorescence microscopy (Nikon Microscope Eclipse 80i). Sterilized samples were left overnight at 37ºC and 5% CO_2 growth medium (DMEM, 10% FBS, 1% P/S) to allow protein adsorption and surface functionalization. Culture medium was then renewed and C2C12 cells were seeded at a 5000 cells/cm^2 density on the materials' surface (3,8 cm^2). After 24 h of culture, wells were rinsed with Dulbecco's phosphate buffered saline (DPBS) and fixed with a 4% paraformaldehyde solution (1 h at room temperature). Samples were then permeabilized with 0.5% Triton-X-100/DPBS, blocked with 5% horse serum (HS) in DPBS (1 h, 37 ºC) and stained with fluorescent Phalloidin (dil:1:100, Invitrogen/ThermoFisher A12379). Finally, samples were mounted in Vectashield mounting media (Palex Medical) and observed through a fluorescence microscope. Image quantification of cell areas (actin cytoskeleton) was performed on ImageJ software.

2.5.3. Myogenic differentiation

To assess myogenic differentiation, C2C12 cells were seeded in growth medium at 20,000 cells/cm^2 on the materials' surface (3,8 cm^2), previously pre-treated with overnight incubation with growth medium to facilitate protein adsorption. After 24 h of culture the medium was changed to supplemented differentiation medium containing insulin transferrin selenium (ITS liquid media supplement, Sigma) (DMEM, 1% ITS, 1% P/S) for 6 days, with medium changes every 2 days. Cells were then fixed with paraformaldehyde for 1 h and blocked with 5% HS in DPBS for 1 h, permeabilized with 0,5% Triton-X-100 in DPBS and incubated with sarcomeric α-actinin mouse monoclonal antibody (Invitrogen/Thermofisher MA1–22863, clone EA-53, 1:200) for 1 h at 37 ºC. Then, samples were rinsed with DPBS and incubated with secondary Alexa 488 conjugated goat anti-mouse IgG polyclonal antibody (Invitrogen/Thermofisher A11029, 1/500) for 1 h at 37 ºC. Finally, samples were mounted with Vectashield containing DAPI and analysed

by fluorescence microscopy. Image quantification of myogenic differentiation was performed on ImageJ software.

The nanohybrid hydrogels with rGO nanosheets showed a strong auto fluorescence background on the same wavelength as DAPI (358/461 nm, blue), hindering the correct visualization of the cell nucleus. To overcome this issue and be able to adequately identify the differentiated myoblasts (myotubes), an adapted method from Inoue et al. [34] was used. The average area of myotubes with two nuclei from the semi-IPN hydrogel (average area: 550 μm^2), which did not show auto fluorescence background and cell nuclei could be observed by DAPI staining, was first calculated. Differentiated myoblasts were considered as those with cell area $\geq$ 550 μm^2 and elongate shape while undifferentiated cells remained with round shape. Myogenic differentiation was quantified as the number of myotubes/cm^2, mean myotube area and diameter and the ratio between the areas of myotubes and the area of total sarcomeric α-actinin positive cells.

2.6. Statistical analysis

One-way ANOVA tests were performed on GraphPad Prism 8.0.2 software. Data were presented as mean ± standard deviation. Statistical significance was indicated by (*) $p < 0.05$, (**) $p < 0.01$, and (***) $p < 0.001$ according to the analysis of variance.

3. Results and discussion

3.1. Microstructure (SEM and AFM results)

HRFESEM images (Fig. 1b) show the cross-section and surface morphology of the semi-IPN and nanohybrid hydrogels with incorporated rGO nanosheets (0.5% and 2% wt/wt) previously swollen in water and freeze-dried to preserve the porous structure. The images show a uniform structure in all samples (no evidence of phase separation is observed), with micropores along the cross-section (Fig. 1b, left column), with pore size < 0.25 μm. This small pore size is related to a very compact structure, which indicates that the system is highly crosslinked.

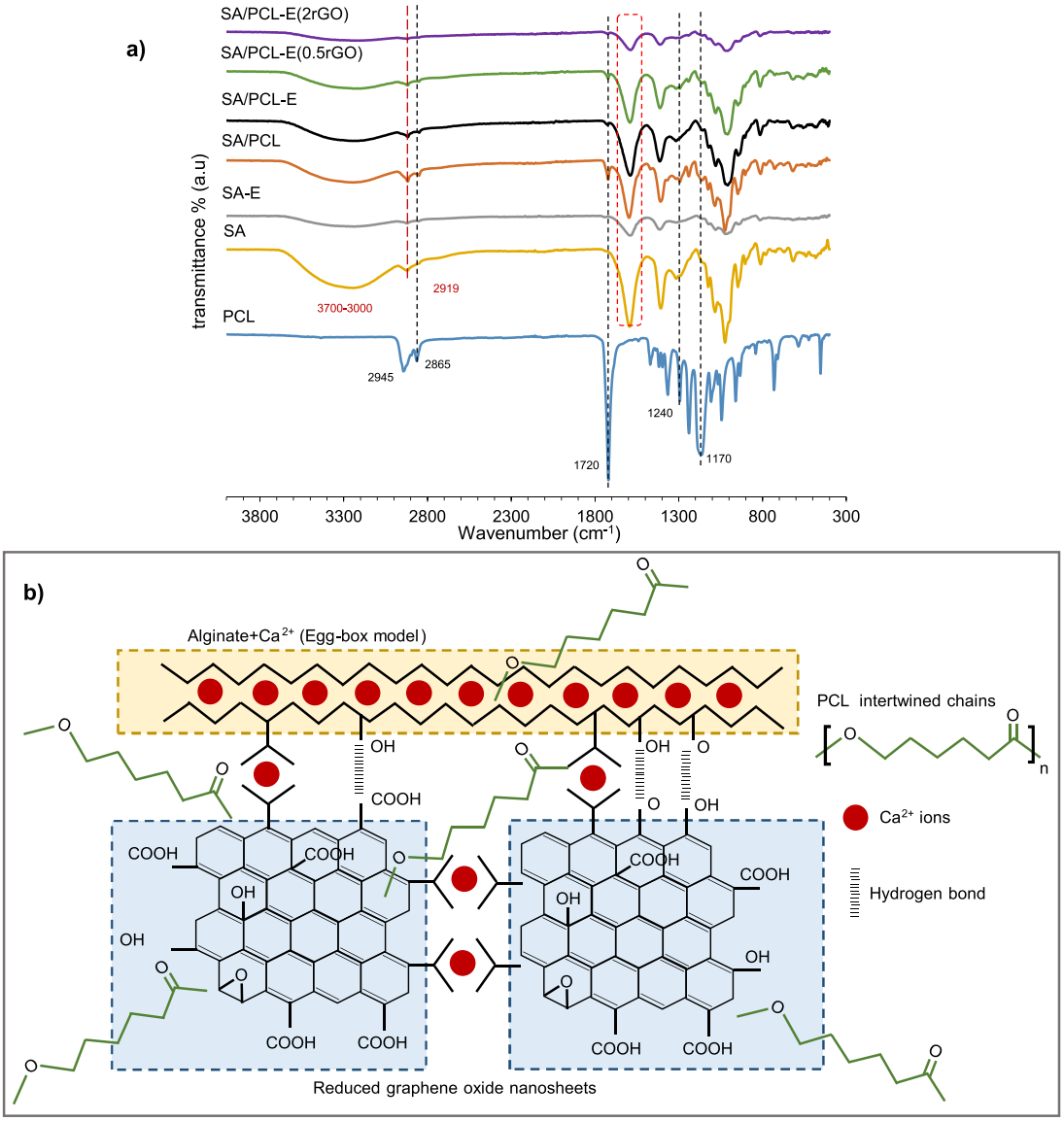

Fig. 2. (a) Fourier transform infrared spectroscopy (FTIR) spectra in the region 4000–300 cm^{-1}: SA/PCL blend, semi-IPN SA/PCL (SA/PCL-E) and nanohybrid composites with 0.5% and 2% of rGO nanosheets. Neat PCL and SA, crosslinked SA (SA-E) have been included as reference. (b) Schematic diagram of the structure of nanohybrid hydrogels.

This feature is expected to limit the swelling capacity and the formation of large pores, as will be verified in the swelling assay (Section 3.3). A homogenous surface, with low porosity, can be observed in the semi-IPN and nanohybrids hydrogels (Fig. 1b, right column) with a slight increase in surface roughness after the incorporation of rGO nanosheets. In addition, the image of pristine rGO nanosheets after dispersion in water by ultrasonic bath shows that their length can reach 3–4 μm and that they tend to wrinkle, forming small aggregates. The surface roughness observed in the nanohybrid hydrogels suggests the presence of rGO nanosheets close to the surface highly embedded in the polymeric matrix.

Dry samples obtained after solvent casting were analysed by AFM to study the surface topography (Fig. 1c). The porous alginate-based hydrophilic structures collapsed during drying, as expected (see Fig. 3 in ref [35]). On the nanoscale, the surfaces of the semi-IPN and nanocomposites with rGO nanosheets show a fairly homogeneous structure with rough areas, as can be seen in Fig. 1c, consistent with the presence of two materials and two solvents (water and dioxane) with different evaporation dynamics during sample preparation. The roughness parameter, R_q, rises from 4.14 nm for the semi-IPN SA/PCL-E to 9.33 nm for the nanocomposite with 2% of rGO nanosheets.

3.2. Fourier transform infrared spectroscopy analysis

Fig. 2a shows the FTIR spectra of neat PCL, SA, SA/PCL blend and semi-IPN SA/PCL-E with and without rGO nanosheets. The neat PCL spectrum shows the characteristic peaks related to asymmetric and symmetric stretching of the CH_2 groups, which belong to the bands at 2945 and 2865 cm^{-1} [36,37]. The distinctive peak around 1720 due to carbonyl stretching of the –COOH group can be clearly identified, together with asymmetric COC stretching at 1240 cm^{-1} and symmetric COC stretching at 1170 cm^{-1} [37,38]. Neat SA shows a wide band between 3700 and 3000 cm^{-1} associated with O-H stretching. The peaks at 2919 cm^{-1} and 1417 $cm^{-1}$are due to C–H stretch sp^3 and C-OH stretch, respectively [39,40]. Alginate gelation takes place when divalent ions interact ionically with the guluronic acid block, which produce a three-dimensional network [41]. Crosslinking SA replaces sodium with calcium ions, resulting in a change in ion density, diameter and weight, affecting the stretch forces applied to the C═O carboxylic salt functional groups [42]. This phenomenon can be identified as a slight shift from 1593 cm^{-1} in pristine SA to 1590 cm^{-1} in the crosslinked samples [39,43].

The SA/PCL blend spectrum shows the characteristic peaks related to both SA and PCL, confirming their presence in the blend. The semi-IPN (SA/PCL-E) obtained after crosslinking SA with $CaCl_2$ also shows the slight shift related to the stretch in the C═O carboxylic salt functional groups (asymmetric stretching vibrations), with the peak located at 1590 cm^{-1}. After the addition of rGO nanosheets, the position and intensity of the main characteristic absorption peaks did not change substantially because they shared the same functional groups and the amount of filler is small. The spectra show a slight reduction of the intensity of the band between 3700 and 3000 cm^{-1}, more noticeable after the addition of 2% of rGO (SA/PCL-E(2rGO) sample) [44]. This behavior suggests an interactions between the polymer matrix and rGO nanoparticles through oxygen-containing functional groups, such as –OH and –COO groups, forming interfacial hydrogen bonds between both components [44]. An additional shift of the peak related to carbonyl stretching (C═O) can be seen in the nanohybrid composites, from 1593 to 1588 cm^{-1}, which may have been produced by further interactions between SA chains and rGO nanosheets through Ca^{2+} ions. Specific ions, such Ca^{2+}, Zn^{2+} and Fe^{3+}, are able to crosslink alginate chains and GO nanosheets simultaneously, generating hydrogels with crosslinked GO networks inside the alginate hydrogel [45–47]. It has also been reported that the oxygen-containing functional groups of GO can bond to divalent ions, particularly Mg^{2+} and Ca^{2+} [48]. The nanocomposite spectra suggest that although the number of functional groups in rGO nanosheets is lower than in GO, they still remain.

We therefore hypothesized that the nanocomposites present a complex nano-network structure (Fig. 2b) formed by bonds between SA chains induced by Ca^{2+} ions (the well-known *egg-box* structure [49]), links between rGO nanosheets and SA chains and also between rGO nanosheets themselves through Ca^{2+} ions, and finally hydrogen bonds between rGO nanosheets and SA chains (-OH and –COOH groups). In this structure, the PCL chains are trapped inside the calcium alginate-rGO nano-network. The results of the characterization of the system using additional techniques are presented below. These confirmed the proposed structure of the nanohybrid hydrogels.

3.3. Swelling behavior and surface wettability

Water sorption (Fig. 3a) was obtained gravimetrically as the amount of water absorbed from the dry to the swollen state in crosslinked samples (SA/PCL-E and nanohybrid hydrogels). Crosslinked alginate (SA-E) was included as reference. The swelling degree of the systems is moderate (between 50% and 70%), indicating high crosslinking density. The mean swelling degree in the semi-IPN SA/PCL-E does not present

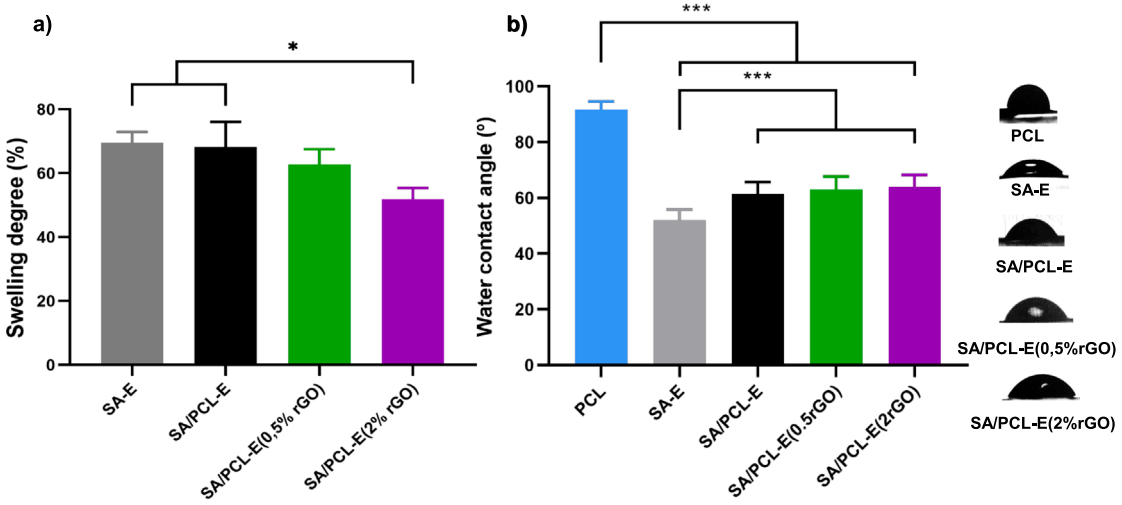

Fig. 3. (a) Swelling degree in equilibrium. (b) Water contact angle of semi-IPN SA/PCL-E and nanohybrid hydrogels with 0.5% and 2% of rGO. Crosslinked SA (SA E) and PCL have been included as reference. Graphs show mean ± standard deviation. (*) and (***) indicate significant differences ($p < 0.05$ and $p < 0.001$, respectively).

significant differences with respect to the crosslinked alginate, probably due to the fact that the system is highly crosslinked and the amount of PCL is low. The addition of rGO nanosheets affects the swelling capacity as expected, according to previous water sorption results obtained with other composite hydrogels of alginate/carbon nanomaterials [2,35]. Nanohybrids with 0.5% of rGO did not show a statistically significant reduction of water swelling. However, the nanohybrids with 2% of rGO exhibited a statistically significant decrease of 16% with respect to the swelling degree of the semi-IPN SA-E. These results are in good agreement with the porous microstructure shown in Fig. 1b (cross-section images), where the small pore size shown by the semi-IPN and the nanohybrid hydrogels results in moderate swelling capacity.

Fig. 3b shows the surface wettability obtained from the static water contact angle measurement. The contact angle for the reference samples is 92 ± 3º for smooth surface PCL (low wettability) [50] and 52 ± 4º for crosslinked SA. In the semi-IPN SA/PCL with 10% PCL, the contact angle increases to 61 ± 4º. The addition of rGO nanosheets does not significantly influence the hydrophilic behavior of the nanohybrid composites, in good agreement with previous results [51].

The reduced swelling in the nanohybrid hydrogels suggest that the remaining functional groups of rGO nanosheets (after reduction) embedded in the SA/PCL matrix are able to generate a more compact network [46,52], consistent with the structure proposed in the previous section. However, surface wettability is not altered, probably due to the particles being completely covered by the polymer matrix and not showing up on the surface.

3.4. Thermal behavior and degradation, and mechanical properties

3.4.1. Differential scanning calorimetry (DSC)

Fig. 4a shows the normalized heat flow on heating. SA/PCL blend shows a small endotherm peak around 60 ºC followed by a large one at 180 ºC; finally, thermal degradation can be identified at temperatures higher than 220 ºC. Alginates have a strong affinity for water and the molecular structure determines their hydration properties [53]. Water can be released at different temperatures according to the interactions between water and alginate chains [54]. Free water can be released at temperatures lower than 80 ºC, water linked through hydrogen bonds can be released in the interval between 80 and 120 ºC and more tightly linked water through polar interaction with carboxyl groups at higher temperatures [53,55]. The samples were vacuum dried at 60 ºC for 24 h to remove free water, however, in neat SA, crosslinked SA and SA/PCL blend, a peak appeared at temperatures higher than 150 ºC, related to the evaporation of the tightly linked water. This was not found in the semi-IPN SA/PCL and the nanocomposites with rGO nanosheets, indicating their lower hydrophilic character. Both alginate and rGO nanosheets possess -COOH groups that can bond with water molecules and also with each other through hydrogen bonds. The lower intensity of this peak after the ionic crosslinking of the carboxyl groups of alginate and Ca^{2+} ions (samples SA E and SA/PCL E) indicates a reduction of bonded water molecules [47]. In the nanohybrid hydrogels, the endotherm peak related to the evaporation of tightly bonded water molecules can scarcely be seen. This behavior indicates strong links between the SA chain, Ca^{2+} ions and rGO nanosheets, resulting in a high crosslinked network with reduced capacity to bond with water molecules. The results are in good agreement with those obtained from the swelling assay, in which incorporating 2% rGO nanosheets significantly reduced the swelling capacity. These results reinforced the proposed structure of the nanohybrid hydrogels based on complex nano-networks with multiple interactions between the components through Ca^{2+} ions and hydrogen bonding (Fig. 2b).

The melting process in the blend is related to PCL crystallization (only 10% *wt/wt*) and in the semi-IPN and nanohybrid composites. The melting temperature, enthalpy of fusion and crystallinity are collected in Table 2. There are no significant changes in the PCL melting temperature, although the crystallinity of the embedded PCL is strongly affected by alginate chains, ionic crosslinking and rGO nanosheets, hindering the reorganization of the PCL chains (see the dotted box in Fig. 4a). PCL crystallinity in the SA/PCL blend is reduced from $X_C = 0.64$ for neat PCL to $X_C = 0.18$, with an additional reduction after crosslinking ($X_C = 0.1$). The crystallinity continues to decrease after incorporating rGO nanosheets to $X_C = 0.06$ for the nanohybrid composite with 0.5% rGO and 0.04 for the 2% sample.

3.4.2. Thermogravimetry analysis (TGA)

The thermal degradation profile in the SA/PCL blend and the semi-IPN SA/PCL is dominated by the SA profile (Fig. 4b and c), consistent with the 90% SA in the sample. SA, SA/PCL blend and crosslinked samples (SA-E, semi-IPN SA/PCL-E and nanohybrid composites) show an initial weight loss due to the removal of water molecules at temperatures below 200 ºC (free and linked water) [13], in good agreement with the DSC thermogram. The first degradation step occurred in the interval 200–275 ºC followed by a second step in the range between 290 and 525 ºC, both related to the degradation of the SA matrix. The third process was at temperatures above 525 ºC, attributed to the formation of metal carbonates [42,47]. Crosslinking, in both SA and SA/PCL blends shifts the first process of the thermal degradation to higher temperatures. The 50% weight loss temperature, $T_{d\text{-}50\%}$, is more than 30 ºC higher in the crosslinked samples [47]. The nanohybrid composites (Fig. 4d and e) with 0.5% and 2% rGO nanosheets show an additional shift in $T_{d\text{-}50\%}$, ca. 50 ºC, although the degradation profile is quite similar to the semi-IPN. It can therefore be concluded that thermal stability increases after adding both Ca^{2+} ions and rGO nanosheets.

3.4.3. Mechanical properties

The mechanical properties of hydrogels on wet environments (e.g. under in vitro or in vivo conditions) may be completely different from those in the dry state. Thus, the complex modulus (storage modulus (E') and loss modulus (E'')) was obtained in the interval between 35 and 39 ºC, simulating physiological conditions (Fig. 4f). The storage modulus of crosslinked SA is $9.55{\cdot}10^6 \pm 1.1{\cdot}10^5$ Pa, in good agreement with previous results of highly crosslinked calcium alginate films [56]. As expected, the semi-IPN SA/PCL-E shows an increase in the mechanical properties in both E' and E'' ($5.84{\cdot}10^7 \pm 2.6{\cdot}10^6$ Pa and $1.47{\cdot}10^7 \pm 5.9{\cdot}10^5$ Pa, respectively) due to the presence of 10% of PCL, which possess higher mechanical strength. This enhancement in the mechanical properties indicates that the PCL chains are homogeneously dispersed in the alginate network, reinforcing its structure. It can be observed that the addition of rGO nanosheets affects the mechanical properties of the polymeric matrix, though not in the same manner. The nanohybrid hydrogel with 0.5% of rGO shows a substantial rise in the storage modulus and loss modulus ($2.28{\cdot}10^8 \pm 1.1{\cdot}10^7$ Pa and $4.92{\cdot}10^7 \pm 2.4{\cdot}10^6$ Pa, respectively). However, the addition of 2% of rGO does not increase the mechanical behavior ($E' = 3.70{\cdot}10^7 \pm 1{\cdot}10^6$ Pa and $E'' = 7.87{\cdot}10^6 \pm 2.2{\cdot}10^5$ Pa), but even decrease slightly its value. This deterioration of the mechanical properties may be attributed to the aggregation of rGO during the preparation of the nanohybrid hydrogel with higher amount of nanosheets. These results are consistent with other studies with graphene-based nanocomposites, where the increasing concentration of GO or rGO produced a decline in the mechanical properties [57,58] due to a poor dispersion of the nanoparticles in the composite matrix.

3.5. Electrical conductivity

rGO nanosheets were introduced into the semi-IPN SA/PCL-E with the aim of increasing its conductive properties. Conductivity was measured at frequencies of 20, 50 and 100 kHz in dry samples (Fig. 4g). The semi-IPN SA/PCL-E has low conductivity, which increases significantly after adding rGO nanosheets, which have been reported to promote electronic conduction across the entire range of frequencies [59,60]. At 100 kHz, conductivity rises from 0.43 mS/m for the semi-IPN

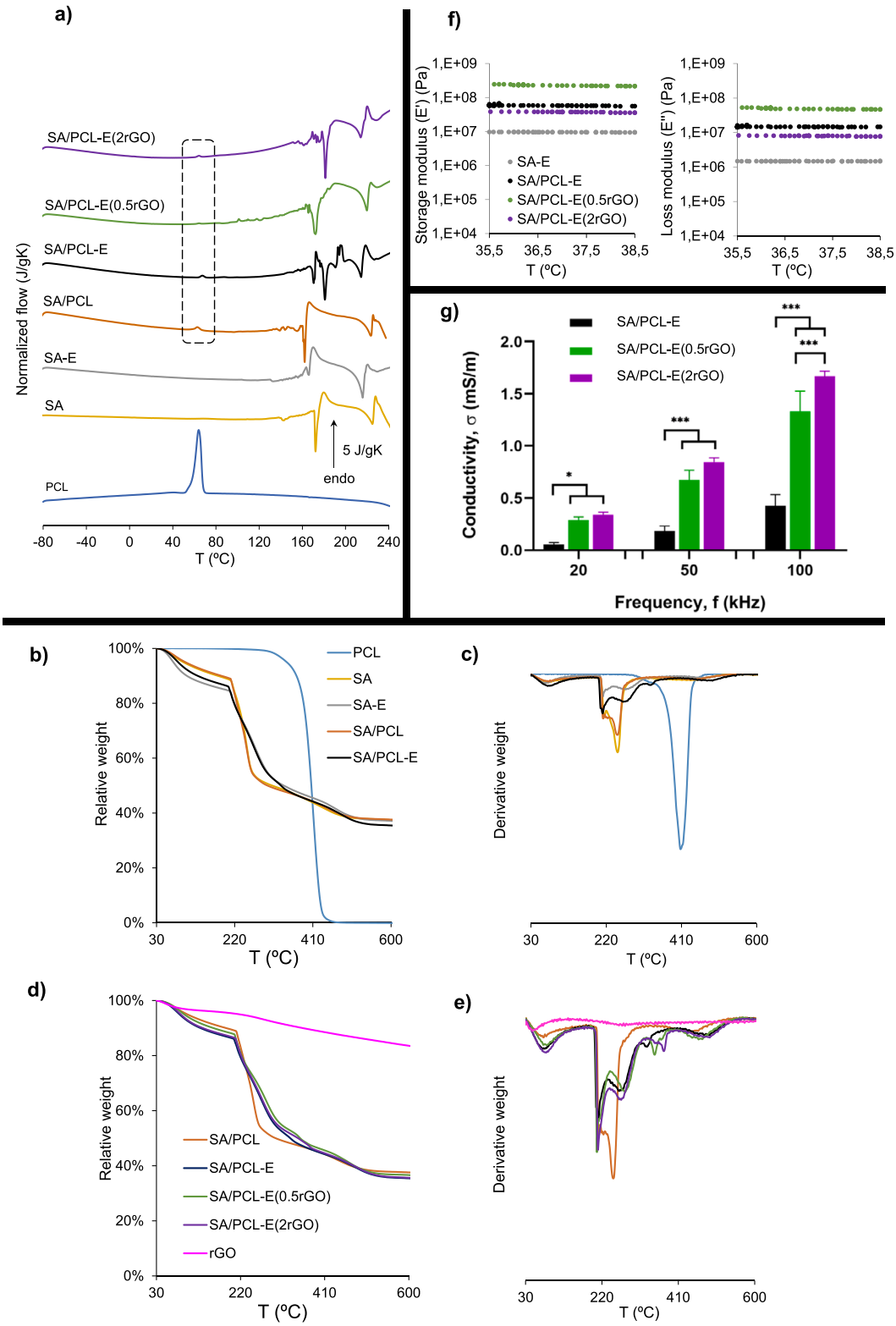

Fig. 4. (a) DSC thermograms at a rate of 20 °C/min. Normalized heat flow on heating of SA/PCL blend, semi-IPN SA/PCL (SA/PCL-E) and nanohybrid composites with 0.5% and 2% of rGO nanosheets. Thermogravimetry results (TGA): (b) SA/PCL blend, semi-IPN SA/PCL (SA/PCL-E) and (c) derivative. (d) Nanohybrid hydrogels with 0.5% and 2% of rGO and (e) derivative. SA/PCL-E has been also included in (d) and (e) to facilitate comparison. Neat SA and PCL and crosslinked SA (SA-E) have been included as reference in DSC and TGA results. (f) Dynamic mechanical analysis. Storage modulus (E') and loss modulus (E'') in the interval 35–39 ºC performed on samples immersed in water. (g) Electrical conductivity of semi-IPN SA/PCL (SA/PCL-E) and nanohybrid composites with 0.5% and 2% of rGO nanosheets at different frequencies (20, 50 and 100 kHz). Graph shows mean ± standard deviation. (*), (**) and (***) indicate significant differences ($p < 0.05$, $p < 0.01$ and $p < 0.001$, respectively).

Table 2
50% weight loss decomposition temperature from the thermogravimetric assay ($T_{d\text{-}50\%}$). Melting temperature (T_m), enthalpy of fusion (ΔH_f) and degree of crystallinity related to PCL content (from DSC thermograms).

Sample	$T_{d\text{-}50\%}$ (°C)	T_m (°C)	ΔH_f (J/g)	X_c PCL
PCL	405	64.5	89.8	0.64
SA	311	–	–	–
SA-E	339	–	–	–
SA/PCL	299	62.8	2.68	0.18
SA/PCL-E	332	67.3	1.4	0.1
SA/PCL-E(0.5rGO)	351	64.2	0.9	0.06
SA/PCL-E(2rGO)	350	64.2	0.6	0.04

SA/PCL to 1.33 mS/m for the nanohybrid 0.5% rGO composite and to 1.67 mS/m after adding 2% rGO nanosheets, although without reaching the percolation threshold. The results suggest possible aggregation of the rGO nanosheets, more noticeable at the higher concentration, which moderately increases conductivity in this sample (in good agreement with DMTA results). The conductivity obtained for the nanohybrid hydrogels is in the same range as other electroactive biomaterials for tissue engineering applications that have induced a cell response [61,62] and those recommended specifically for skeletal muscle applications ($8.0 \times 10^{-4} \sim 4.5 \times 10^{-3}$ S/m) [63].

3.6. Biocompatibility

It is essential to evaluate the biomaterial cytotoxicity for biomedical applications, which was assessed for murine myoblast (C2C12 cell line) exposed to the extracts of the semi-IPN SA/PCL-E and the nanohybrid hydrogels. Both components of the polymer matrix, SA and PCL are biocompatible and biodegradable polymers widely used in the biomedical field [64–66]. However, the cytotoxicity of carbon nanomaterials such as graphene, GO or rGO have been reported to depend not only on the concentration but to a large extent on the processing techniques used to prepare the biomaterial [67].

Fig. 5a shows the cytotoxicity results after 24, 48 and 72 h exposure to the extracts. According to the ISO standard 109935, the materials are considered cytotoxic when cell viability shows values lower than 70% than the negative control. The semi-IPN SA/PCL-E and the nanohybrid hydrogels have viability values over 80% in the three evaluated times, with no significant differences from the negative control (considered as 100% viability). This allows us to conclude that the materials are biocompatible, in good agreement with previous results in which rGO nanoparticles entrapped in polymeric matrices [68,69] were not cytotoxic even at concentrations higher than those administered in form of a solution [70].

3.7. Myoblast adhesion on semi-IPN SA/PCL-E and nanohybrid hydrogels

Cell adhesion was studied after 24 h of culture on samples preconditioned with protein adsorbed on the surface (Fig. 5b and c). Myoblasts C2C12 were seeded at a low density (5000 cells/cm^2) to minimize cell contact. Actin staining showed that the average cell area increases significantly in the semi-IPN SA/PCL-E (mean cell area ca. 1190 μm^2) compared to the SA-E hydrogel, included as reference (mean cell area ca. 930 μm^2). The surface of hydrogels are known to show poor cell adhesion due to poor mechanical properties, high hydrophilicity or the absence of binding sites [5,71]. High hydrophilicity hinders protein absorption on the biomaterial surface, a key factor in regulating cell behavior [72–75], which can be overcome by combining the hydrogel with a hydrophobic polymer. Optimal hydrophilicity has been reported to enhance cell adhesion [76], which is maximized on surfaces with moderate wettability (50–70°). The wettability of the semi-IPN SA/PCL, which contains 10% of PCL, is significantly lower than that of the SA-E hydrogel (as shown by the increase in the water contact angle), which is at the limit of what is considered moderate surface wettability. The rise in the cell area in the semi-IPN SA/PCL-E seems to be related to reduced surface hydrophilicity, which facilitates protein adsorption and increases bioactivity, improving cell adhesion.

After adding rGO, there was a clear trend towards higher average cell area (Fig. 5b). Both nanohybrid hydrogels (with 0.5% and 2% of rGO nanosheets) present significant differences in their average cell area to the SA-E hydrogel. The nanohybrid hydrogel with 2% rGO increases ca.

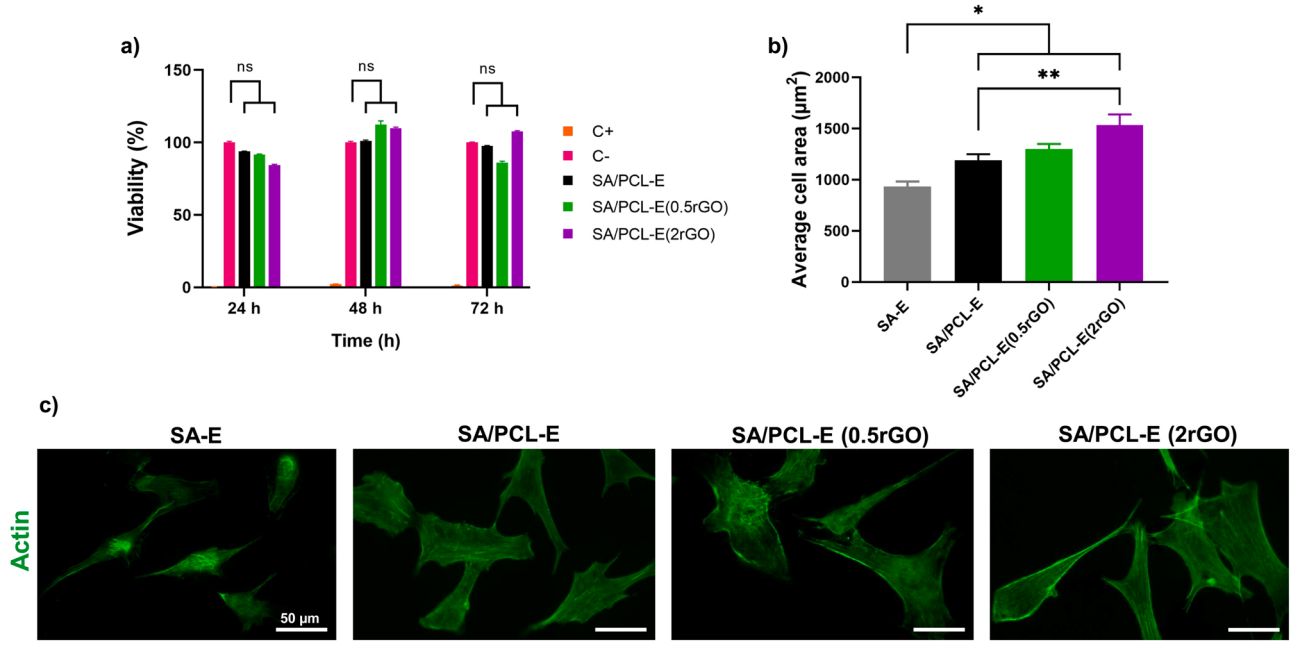

Fig. 5. Cytotoxicity results and cell adhesion. (a) MTT cytotoxicity results represented as cell viability after 24, 48 and 72 h incubation with extracts from semi-IPN and nanohybrid hydrogels with 0.5% and 2% of rGO nanosheets. Positive control: latex extract, negative control: growth medium. (b) Average cell adhesion area for each condition from actin staining. (c) Representative immunofluorescence images of cells attached to the different hydrogels (actin staining). SA-E was considered as reference. Graphs show mean ± standard deviation. (*), (**) and (***) indicate significant differences ($p < 0.05$, $p < 0.01$ and $p < 0.001$, respectively).

by 65% and 28% with respect to the SA-E hydrogel and the semi-IPN SA/PCL-E, respectively. It has been shown that cell adhesion is enhanced in rGO-based hybrid nanomaterials [77–79]. It has also been hypothesized that rGO enables certain proteins from the culture medium to be adsorbed on the rGO surface, promoting cell adhesion [79,80]. Protein absorption is highly dependent on the physicochemical properties of the surfaces and interactions such as electrostatic forces, hydrophobic interactions and hydrogen bonding [80,81]. rGO nanosheets are able to form hydrogen bonds with proteins through oxygenous groups along with electrostatic forces and hydrophobic interactions [80]. The results obtained suggest that the higher cell-spreading during adhesion in the nanohybrid hydrogels after adding rGO could be related to enhanced adsorption of proteins involved in cell adhesion onto the surface of rGO-containing hydrogels.

3.8. Myoblast differentiation on semi-IPN SA/PCL-E and nanohybrid hydrogels

Fig. 6 shows immunofluorescence images (Fig. 6a) and the quantification of myoblast differentiation on the semi-IPN and nanohybrid hydrogels with rGO nanosheets assessed after 6 days of culture in ITS-containing medium (Fig. 6b to e). Differentiation medium was specifically used to analyze whether, under culture conditions that favor cell differentiation, the conductive properties of the nanohybrid hydrogels stimulate myogenesis.

The semi-IPN SA/PCL-E shows a dramatic rise in myogenic differentiation of C2C12 cells compared to the SA-E hydrogel (included as reference), with a 400% increase in the number of myotubes/cm^2 (Fig. 6b). The ratio between the area of the myotubes and the sarcomeric α-actinin positive cells in the semi-IPN is also more than twice the ratio in the SA-E hydrogel (Fig. 6d). The morphology of the myotubes is also affected; the average myotube area and diameter in the semi-IPN is respectively 280% and 150% higher compared to the values obtained in the SA-E hydrogel (Fig. 6c and e). These results indicate that the cell-adhesion behavior, with a higher cell-spreading area, is reflected in cell differentiation, as reported elsewhere [72,82]. The reduced surface hydrophilicity (increased water contact angle) promotes adsorption of proteins, among them cell adhesive glycoproteins (such as fibronectin and laminin), which in turn, enhances cell adhesion (larger spreading areas) and stimulates cell differentiation [72,75].

The nanohybrids hydrogels with 0.5% and 2% rGO nanosheets also show considerably more myoblast differentiation than both the SA-E hydrogel and the semi-IPN SA/PCL-E without nanoparticles (Fig. 6a). Conducting cell substrates have been shown to promote myogenic differentiation [54,83,84]. The conductivity in both nanohybrid hydrogels increased substantially after adding rGO nanoparticles, as can be seen in Fig. 4f. The nanohybrid hydrogels with 2% rGO shows significant differences in cell differentiation in all the parameters analysed. The number of myotubes per cm^2 increase by 700% compared to the SA-E hydrogel and almost 200% as compared with the semi-IPN SA/PCL (Fig. 6b). The ratio between the area of the myotubes and the sarcomeric α-actinin positive cells in this nanohybrid hydrogel is also more than four times the ratio in the SA-E hydrogel and almost twice the ratio in the semi-IPN SA/PCL-E (Fig. 6d).

Regarding the morphology, the average area of the myotubes and the diameter show a 180% and 150% increase, respectively, compared to the semi-IPN SA/PCL (Fig. 6c and e). The nanohybrid hydrogels with 0.5% rGO nanosheets also show an improvement in terms of myogenic differentiation. The results, although not as marked as with 2% rGO, indicate that the average area of myotubes increases significantly. These results are in good agreement with those reported in several previous studies, where it has been suggested that electrically conductive environments, even without external electrostimulation, facilitate electrical communication between myoblasts, leading to increased myogenic differentiation [15,51,59]. The polymeric matrix served as elastomeric environment and rGO provided the electric conductivity. The better

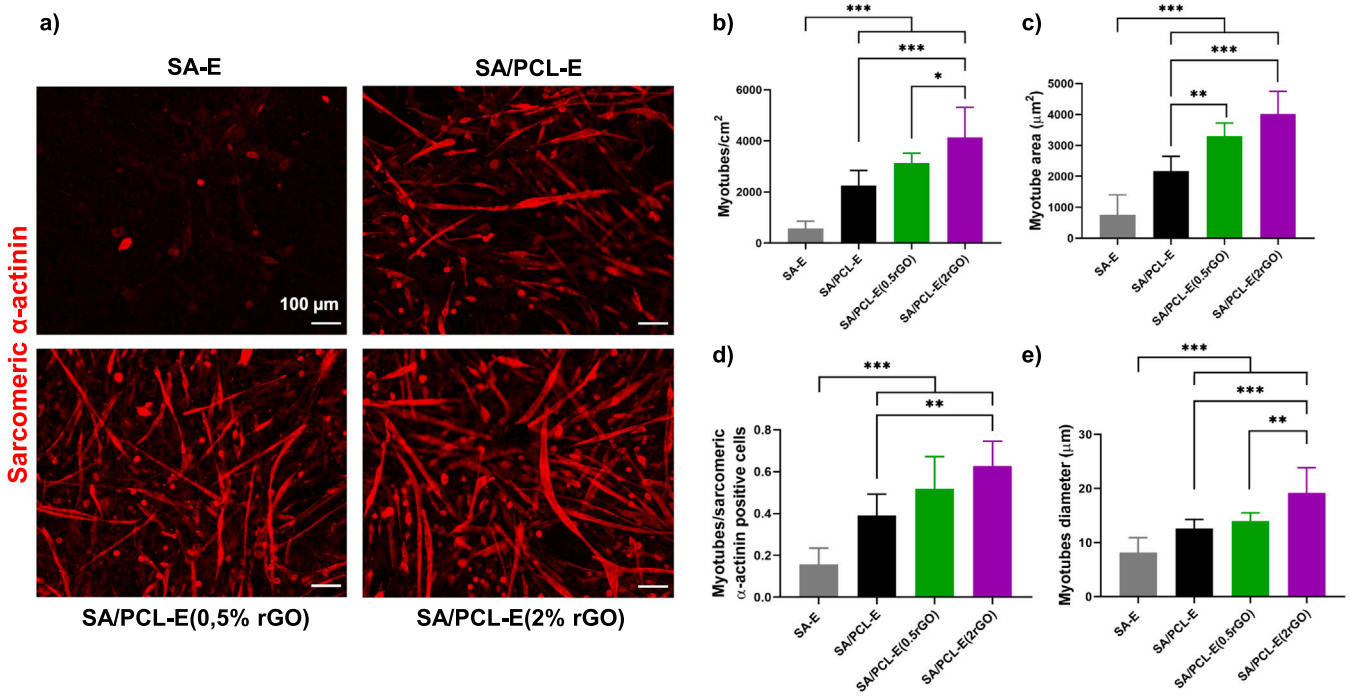

Fig. 6. Results of myoblast differentiation. (a) Immunofluorescence images of differentiated myoblasts (sarcomeric α-actinin staining) after 6 days of culture in differentiation medium (DMEM+1% P/S+1%ITS). (b) Myotubes density represented as number of myotubes/cm^2. (c) Average myotubes area. (d) Ratio between the area of differentiated myotubes/area of total sarcomeric α-actinin positive cells. (e) Mean diameter of myotubes after analysis of 80 random myotubes per hydrogel. SA-E was considered as reference. Graphs show mean ± standard deviation. (*), (**) and (***) indicate significant differences ($p < 0.05$, $p < 0.01$ and $p < 0.001$, respectively).

myoblast differentiation in the nanohybrid hydrogels than in the semi-IPN SA/PCL-E could be attributed to the increased conductivity of the cell substrate after adding rGO nanoparticles to the polymeric matrix. It should be noted that even under conditions that favor myogenic differentiation (myogenic culture medium), the conductive properties of rGO stimulate myogenesis over and above what occurs with cell substrates without conductive properties.

These results demonstrate that the combination of calcium alginate and a very small amount of PCL in the form of semi-IPN and rGO produce stable conductive nanohybrid hydrogels with enhanced physical and biological properties that show great promise for muscle tissue engineering, in good agreement with our hypothesis.

4. Conclusions

We developed electroactive cell substrates consisting of a novel semi-IPN SA/PCL crosslinked with Ca^{2+} ions and rGO nanosheets (0.5% and 2% wt/wt rGO nanosheets) to assess its potential to stimulate cell adhesion and myogenic differentiation. Freeze-dried samples showed a homogeneous porous structure with an increase in surface roughness after adding rGO nanosheets. The FTIR, calorimetry and swelling results suggest the formation of a complex nano-network structure formed by bonds between SA chains induced by Ca^{2+} ions (*egg-box* model), links between rGO nanosheets and SA chains and also between rGO nanosheets themselves through Ca^{2+} ions and strong hydrogen bonding between rGO nanosheets and SA chains. Thermal stability was improved both after crosslinking through Ca^{2+} ions and incorporating rGO nanosheets. The resulting electric conductivity of the nanohybrid hydrogels is expected to be suitable for electroactive tissues, including skeletal muscle. The in vitro biological studies with murine myoblasts revealed that the nanohybrid hydrogels are not cytotoxic and can greatly promote myoblast adhesion and myogenic differentiation. These novel nanohybrid hydrogels have shown to be promising biomaterials for the development of biomedical applications, particularly in skeletal muscle tissue engineering. Regeneration of electroactive tissues like neural and cardiac ones, are also potential applications of the nanohybrid biomaterials engineered, however, further studies are needed to explore their full potential.

CRedit authorship contribution statement

J.L. Aparicio-Collado: Experiments, Data curation, Formal analysis, Investigation, Writing – reviewing and editing. **N. García-San Martín:** Experiments, Data curation. **J. Molina-Mateo:** Formal analysis, Investigation, Funding acquisition. **C. Torregrosa Cabanilles:** Formal analysis, Investigation. **V. Donderis Quiles:** Experiments, Data curation. **Á. Serrano-Aroca:** Conceptualization, Supervision, Writing – reviewing and editing, Funding acquisition. **R. Sabater i Serra:** Conceptualization, Supervision, Writing – reviewing and editing, Funding acquisition.

Declaration of Competing Interest

The authors declare that they have no known competing financial interests or personal relationships that could have appeared to influence the work reported in this paper.

Acknowledgments

Financial support from the Spanish Ministry of Science and Innovation (MCIN (Spain), AEI/FEDER funds) through the projects RTI2018-097862-B-C21 and PID2020-119333RB-I00/AEI/10.13039/501100011033 are acknowledged. CIBER-BBN initiative is funded by the VI National R&D&I Plan 2008–2011, Iniciativa Ingenio 2010, Consolider Program. CIBER actions are financed by the Instituto de Salud Carlos III (Spain) with assistance from the European Regional Development Fund.

References

[1] X. Sun, C. Ma, W. Gong, Y. Ma, Y. Ding, L. Liu, Biological properties of sulfanilamide-loaded alginate hydrogel fibers based on ionic and chemical crosslinking for wound dressings, Int. J. Biol. Macromol. 157 (2020) 522–529, https://doi.org/10.1016/j.ijbiomac.2020.04.210.

[2] M. Llorens-Gámez, Á. Serrano-Aroca, Low-cost advanced hydrogels of calcium alginate/carbon nanofibers with enhanced water diffusion and compression properties, Polymers 10 (2018) 405, https://doi.org/10.3390/polym10040405.

[3] Á. Serrano-Aroca, M. Ferrandis-Montesinos, R. Wang, Antiviral properties of alginate-based biomaterials: promising antiviral agents against SARS-CoV-2, ACS Appl. Bio Mater. 4 (2021) 5897–5907, https://doi.org/10.1021/acsabm.1c00523.

[4] M. Llorens-Gámez, B. Salesa, Á. Serrano-Aroca, Physical and biological properties of alginate/carbon nanofibers hydrogel films, Int. J. Biol. Macromol. 151 (2020) 499–507, https://doi.org/10.1016/j.ijbiomac.2020.02.213.

[5] A.A. Abalymov, B.V. Parakhonskiy, A.G. Skirtach, Colloids-at-surfaces: physicochemical approaches for facilitating cell adhesion on hybrid hydrogels, Colloids Surf. A Physicochem. Eng. Asp. 603 (2020) 1–11, https://doi.org/10.1016/j.colsurfa.2020.125185.

[6] J.A. Rowley, G. Madlambayan, D.J. Mooney, Alginate hydrogels as synthetic extracellular matrix materials, Biomaterials 20 (1999) 45–53, https://doi.org/10.1016/S0142-9612(98)00107-0.

[7] J.L. Aparicio-Collado, J.J. Novoa, J. Molina-Mateo, C. Torregrosa-Cabanilles, Á. Serrano-Aroca, R. Sabater, I. Serra, Novel semi-interpenetrated polymer networks of poly(3-hydroxybutyrate-co-3-hydroxyvalerate)/poly (vinyl alcohol) with incorporated conductive polypyrrole nanoparticles, Polymers 13 (2021) 1–21, https://doi.org/10.3390/polym13010057.

[8] M. Martí, B. Frígols, B. Salesa, Á. Serrano-Aroca, Calcium alginate/graphene oxide films: reinforced composites able to prevent Staphylococcus aureus and methicillin-resistant Staphylococcus epidermidis infections with no cytotoxicity for human keratinocyte HaCaT cells, Eur. Polym. J. 110 (2019), https://doi.org/10.1016/j.eurpolymj.2018.11.012.

[9] R. Dwivedi, S. Kumar, R. Pandey, A. Mahajan, D. Nandana, D.S. Katti, D. Mehrotra, Polycaprolactone as biomaterial for bone scaffolds: review of literature, J. Oral. Biol. Craniofac. Res. 10 (2020) 381–388, https://doi.org/10.1016/j.jobcr.2019.10.003.

[10] D. Mondal, M. Griffith, S.S. Venkatraman, Polycaprolactone-based biomaterials for tissue engineering and drug delivery: current scenario and challenges, Int. J. Polym. Mater. Polym. Biomater. 65 (2016) 255–265, https://doi.org/10.1080/00914037.2015.1103241.

[11] D. Mondal, M. Griffith, S.S. Venkatraman, Polycaprolactone-based biomaterials for tissue engineering and drug delivery: current scenario and challenges, Int. J. Polym. Mater. Polym. Biomater. 65 (2016) 255–265, https://doi.org/10.1080/00914037.2015.1103241.

[12] N. Siddiqui, S. Asawa, B. Birru, R. Baadhe, S. Rao, PCL-based composite scaffold matrices for tissue engineering applications, Mol. Biotechnol. 60 (2018) 506–532, https://doi.org/10.1007/s12033-018-0084-5.

[13] N. Tyagi, K. Gambhir, R. Pandey, G. Gangenahalli, Y.K. Verma, Minimizing the negative charge of alginate facilitates the delivery of negatively charged molecules inside cells, J. Polym. Res. 29 (2022), https://doi.org/10.1007/s10965-021-02813-6.

[14] A.L. Rivera-Briso, F.L. Aachmann, V. Moreno-Manzano, Á. Serrano-Aroca, Graphene oxide nanosheets versus carbon nanofibers: enhancement of physical and biological properties of poly(3-hydroxybutyrate-co-3-hydroxyvalerate) films for biomedical applications, Int. J. Biol. Macromol. 143 (2020) 1000–1008, https://doi.org/10.1016/j.ijbiomac.2019.10.034.

[15] V. Palmieri, F. Sciandra, M. Bozzi, M. De Spirito, M. Papi, 3D graphene scaffolds for skeletal muscle regeneration: future perspectives, Front. Bioeng. Biotechnol. 8 (2020) 1–8, https://doi.org/10.3389/fbioe.2020.00383.

[16] S.H. Ku, M. Lee, C.B. Park, Carbon-based nanomaterials for tissue engineering, Adv. Healthc. Mater. 2 (2013) 244–260, https://doi.org/10.1002/adhm.201200307.

[17] T. Hwang, Z. Frank, J. Neubauer, K.J. Kim, High-performance polyvinyl chloride gel artificial muscle actuator with graphene oxide and plasticizer, Sci. Rep. 9 (2019) 2–10, https://doi.org/10.1038/s41598-019-46147-2.

[18] K.P. Loh, Q. Bao, P.K. Ang, J. Yang, The chemistry of graphene, J. Mater. Chem. 20 (2010) 2277–2289, https://doi.org/10.1039/b920539j.

[19] P. Bellet, M. Gasparotto, S. Pressi, A. Fortunato, G. Scapin, M. Mba, E. Menna, F. Filippini, Graphene-based scaffolds for regenerative medicine, Nanomaterials 11 (2021) 1–41, https://doi.org/10.3390/nano11020404.

[20] E.A. Lee, S.Y. Kwak, J.K. Yang, Y.S. Lee, J.H. Kim, H.D. Kim, N.S. Hwang, Graphene oxide film guided skeletal muscle differentiation, Mater. Sci. Eng. C 126 (2021), https://doi.org/10.1016/j.msec.2021.112174.

[21] S. Bin Jo, U. Erdenebileg, K. Dashnyam, G.Z. Jin, J.R. Cha, A. El-Fiqi, J.C. Knowles, K.D. Patel, H.H. Lee, J.H. Lee, H.W. Kim, Nano-graphene oxide/polyurethane nanofibers: mechanically flexible and myogenic stimulating matrix for skeletal tissue engineering, J. Tissue Eng. 11 (2020), https://doi.org/10.1177/2041731419900424.

[22] M.S. Kang, J. Il Kang, P. Le Thi, K.M. Park, S.W. Hong, Y.S. Choi, D.W. Han, K. D. Park, Three-dimensional printable gelatin hydrogels incorporating graphene oxide to enable spontaneous myogenic differentiation, ACS Macro Lett. 10 (2021) 426–432, https://doi.org/10.1021/acsmacrolett.0c00845.

[23] Y.C. Shin, S.H. Kang, J.H. Lee, B. Kim, S.W. Hong, D.W. Han, Three-dimensional graphene oxide-coated polyurethane foams beneficial to myogenesis, J. Biomater. Sci. Polym. Ed. 29 (2018) 762–774, https://doi.org/10.1080/09205063.2017.1348738.

[24] J.H. Lee, Y. Lee, Y.C. Shin, M.J. Kim, J.H. Park, S.W. Hong, B. Kim, J.W. Oh, K. D. Park, D.W. Han, In situ forming gelatin/graphene oxide hydrogels for facilitated C2C12 myoblast differentiation, Appl. Spectrosc. Rev. 51 (2016) 527–539, https://doi.org/10.1080/05704928.2016.1165686.
[25] A. Patel, Y. Xue, R. Hartley, V. Sant, J.R. Eles, X.T. Cui, D.B. Stolz, S. Sant, Hierarchically aligned fibrous hydrogel films through microfluidic self-assembly of graphene and polysaccharides, Biotechnol. Bioeng. 115 (2018) 2654–2667, https://doi.org/10.1002/bit.26801.
[26] Y.C. Shin, J.H. Lee, L. Jin, M.J. Kim, Y.J. Kim, J.K. Hyun, T.G. Jung, S.W. Hong, D. W. Han, Stimulated myoblast differentiation on graphene oxide-impregnated PLGA-collagen hybrid fibre matrices, J. Nanobiotechnol. 13 (2015) 1–11, https://doi.org/10.1186/s12951-015-0081-9.
[27] K.S. Novoselov, A.K. Geim, S.V. Morozov, D. Jiang, Y. Zhang, S.V. Dubonos, I. V. Grigorieva, A.A. Firsov, Electric field effect in atomically thin carbon films, Science 306 (2004) 666–669, https://doi.org/10.1126/science.1102896.
[28] Y. Zeng, T. Li, Y. Yao, T. Li, L. Hu, A. Marconnet, Thermally conductive reduced graphene oxide thin films for extreme temperature sensors, Adv. Funct. Mater. 29 (2019), 1901388, https://doi.org/10.1002/adfm.201901388.
[29] L.L. Zhang, X. Zhao, M.D. Stoller, Y. Zhu, H. Ji, S. Murali, Y. Wu, S. Perales, B. Clevenger, R.S. Ruoff, Highly conductive and porous activated reduced graphene oxide films for high-power supercapacitors, Nano Lett. 12 (2012) 1806–1812, https://doi.org/10.1021/nl203903z.
[30] L. Yang, W. Weng, X. Fei, L. Pan, X. Li, W. Xu, Z. Hu, M. Zhu, Revealing the interrelation between hydrogen bonds and interfaces in graphene/PVA composites towards highly electrical conductivity, Chem. Eng. J. 383 (2020), 123126, https://doi.org/10.1016/j.cej.2019.123126.
[31] X. Wu, S. Tan, Y. Xing, Q. Pu, M. Wu, J.X. Zhao, Graphene oxide as an efficient antimicrobial nanomaterial for eradicating multi-drug resistant bacteria in vitro and in vivo, Colloids Surf. B Biointerfaces 157 (2017) 1–9, https://doi.org/10.1016/j.colsurfb.2017.05.024.
[32] O.C. Compton, S.T. Nguyen, Graphene oxide, highly reduced graphene oxide, and graphene: versatile building blocks for carbon-based materials, Small 6 (2010) 711–723, https://doi.org/10.1002/smll.200901934.
[33] H. Jo, M. Sim, S. Kim, S. Yang, Y. Yoo, J.H. Park, T.H. Yoon, M.G. Kim, J.Y. Lee, Electrically conductive graphene/polyacrylamide hydrogels produced by mild chemical reduction for enhanced myoblast growth and differentiation, Acta Biomater. 48 (2017) 100–109, https://doi.org/10.1016/j.actbio.2016.10.035.
[34] H. Inoue, K. Kunida, N. Matsuda, D. Hoshino, T. Wada, H. Imamura, H. Noji, S. Kuroda, Automatic quantitative segmentation of myotubes reveals single-cell dynamics of S6 kinase activation, Cell Struct. Funct. 43 (2018) 153–169, https://doi.org/10.1247/csf.18012.
[35] Á. Serrano-Aroca, J.F. Ruiz-Pividal, M. Llorens-Gámez, Enhancement of water diffusion and compression performance of crosslinked alginate films with a minuscule amount of graphene oxide, Sci. Rep. 7 (2017) 1–8, https://doi.org/10.1038/s41598-017-10260-x.
[36] E. Tranquillo, F. Barrino, G. Dal Poggetto, I. Blanco, Sol-gel synthesis of silica-based materials with different percentages of PEG or PCL and high chlorogenic acid content, Materials 12 (2019), https://doi.org/10.3390/ma12010155.
[37] T. Elzein, M. Nasser-Eddine, C. Delaite, S. Bistac, P. Dumas, FTIR study of polycaprolactone chain organization at interfaces, J. Colloid Interface Sci. 273 (2004) 381–387, https://doi.org/10.1016/j.jcis.2004.02.001.
[38] Z. Yang, H. Peng, W. Wang, T. Liu, Crystallization behavior of poly (ε-caprolactone)/layered double hydroxide nanocomposites, J. Appl. Polym. Sci. 116 (2010) 2658–2667, https://doi.org/10.1002/app.
[39] M. Rashtchian, A. Hivechi, S.H. Bahrami, P.B. Milan, S. Simorgh, Fabricating alginate/poly(caprolactone) nanofibers with enhanced bio-mechanical properties via cellulose nanocrystal incorporation, Carbohydr. Polym. 233 (2020), 115873, https://doi.org/10.1016/j.carbpol.2020.115873.
[40] C. Xiao, L. Weng, L. Zhang, Improvement of physical properties of crosslinked alginate and carboxymethyl konjac glucomannan blend films, J. Appl. Polym. Sci. 84 (2002) 2554–2560, https://doi.org/10.1002/app.10582.
[41] S.K. Bajpai, S. Sharma, Investigation of swelling/degradation behaviour of alginate beads crosslinked with Ca2+ and Ba2+ ions, React. Funct. Polym. 59 (2004) 129–140, https://doi.org/10.1016/j.reactfunctpolym.2004.01.002.
[42] T.S. Pathak, J.H. Yun, J. Lee, K.J. Paeng, Effect of calcium ion (cross-linker) concentration on porosity, surface morphology and thermal behavior of calcium alginates prepared from algae (Undaria pinnatifida), Carbohydr. Polym. 81 (2010) 633–639, https://doi.org/10.1016/j.carbpol.2010.03.025.
[43] M. Gomaa, A.F. Hifney, M.A. Fawzy, K.M. Abdel-Gawad, Use of seaweed and filamentous fungus derived polysaccharides in the development of alginate-chitosan edible films containing fucoidan: study of moisture sorption, polyphenol release and antioxidant properties, Food Hydrocoll. 82 (2018) 239–247, https://doi.org/10.1016/j.foodhyd.2018.03.056.
[44] W. Zhao, Y. Qi, Y. Wang, Y. Xue, P. Xu, Z. Li, Q. Li, Morphology and thermal properties of calcium alginate/reduced graphene oxide composites, Polymers 10 (2018) 1–11, https://doi.org/10.3390/polym10090990.
[45] Á. Serrano-Aroca, L. Iskandar, S. Deb, Green synthetic routes to alginate-graphene oxide composite hydrogels with enhanced physical properties for bioengineering applications, Eur. Polym. J. 103 (2018) 198–206, https://doi.org/10.1016/j.eurpolymj.2018.04.015.
[46] H. Zheng, J. Yang, S. Han, The synthesis and characteristics of sodium alginate/graphene oxide composite films crosslinked with multivalent cations, J. Appl. Polym. Sci. 133 (2016), 43616, https://doi.org/10.1002/app.43616.
[47] R. Sabater i Serra, J. Molina-mateo, C. Torregrosa-cabanilles, A. Andrio-Balado, J. Meseguer Dueñas, A. Serrano-Aroca, Bio-nanocomposite hydrogel based on zinc conformation, thermal behavior/degradation, and dielectric properties, Polymers 12 (2020) 702.
[48] S. Park, K.S. Lee, G. Bozoklu, W. Cai, S.B.T. Nguyen, R.S. Ruoff, Graphene oxide papers modified by divalent ions – enhancing mechanical properties via chemical cross-linking, ACS Nano 2 (2008) 572–578, https://doi.org/10.1021/nn700349a.
[49] L. Cao, W. Lu, A. Mata, K. Nishinari, Y. Fang, Egg-box model-based gelation of alginate and pectin: a review, Carbohydr. Polym. 242 (2020), 116389, https://doi.org/10.1016/j.carbpol.2020.116389.
[50] A.O. Šišková, M. Bučková, Z. Kroneková, A. Kleinová, Š. Nagy, J. Rydz, A. Opálek, M. Sláviková, A.E. Andicsová, The drug-loaded electrospun poly(ε-caprolactone) mats for therapeutic application, Nanomaterials 11 (2021), https://doi.org/10.3390/nano11040922.
[51] Y. Du, J. Ge, Y. Li, P.X. Ma, B. Lei, Biomimetic elastomeric, conductive and biodegradable polycitrate-based nanocomposites for guiding myogenic differentiation and skeletal muscle regeneration, Biomaterials 157 (2018) 40–50, https://doi.org/10.1016/j.biomaterials.2017.12.005.
[52] L.C. Jia, W.J. Sun, C.G. Zhou, D.X. Yan, Q.C. Zhang, Z.M. Li, Integrated strength and toughness in graphene/calcium alginate films for highly efficient electromagnetic interference shielding, J. Mater. Chem. C 6 (2018) 9166–9174, https://doi.org/10.1039/c8tc03151g.
[53] A.S. El-Houssiny, A.A. Ward, D.M. Mostafa, S.L. Abd-El-Messieh, K.N. Abdel-Nour, M.M. Darwish, W.A. Khalil, Drug-polymer interaction between glucosamine sulfate and alginate nanoparticles: FTIR, DSC and dielectric spectroscopy studies, Adv. Nat. Sci. Nanosci. Nanotechnol. 7 (2016), 025014, https://doi.org/10.1088/2043-6262/7/2/025014.
[54] R. Dong, X. Zhao, B. Guo, P.X. Ma, Biocompatible elastic conductive films significantly enhanced myogenic differentiation of myoblast for skeletal muscle regeneration, Biomacromolecules 18 (2017) 2808–2819, https://doi.org/10.1021/acs.biomac.7b00749.
[55] P. Laurienzo, M. Malinconico, A. Motta, A. Vicinanza, Synthesis and characterization of a novel alginate-poly(ethylene glycol) graft copolymer, Carbohydr. Polym. 62 (2005) 274–282, https://doi.org/10.1016/j.carbpol.2005.08.005.
[56] R. Russo, M. Malinconico, G. Santagata, Effect of cross-linking with calcium ions on the physical properties of alginate films, Biomacromolecules 8 (2007) 3193–3197, https://doi.org/10.1021/bm700565h.
[57] N. Mansouri, S.F. Al-Sarawi, J. Mazumdar, D. Losic, Advancing fabrication and properties of three-dimensional graphene-alginate scaffolds for application in neural tissue engineering, RSC Adv. 9 (2019) 36838–36848, https://doi.org/10.1039/c9ra07481c.
[58] N. Abzan, M. Kharaziha, S. Labbaf, Development of three-dimensional piezoelectric polyvinylidene fluoride-graphene oxide scaffold by non-solvent induced phase separation method for nerve tissue engineering, Mater. Des. 167 (2019), https://doi.org/10.1016/j.matdes.2019.107636.
[59] H. Jo, M. Sim, S. Kim, S. Yang, Y. Yoo, J.H. Park, T.H. Yoon, M.G. Kim, J.Y. Lee, Electrically conductive graphene/polyacrylamide hydrogels produced by mild chemical reduction for enhanced myoblast growth and differentiation, Acta Biomater. 48 (2017) 100–109, https://doi.org/10.1016/j.actbio.2016.10.035.
[60] N. Mac Kenna, P. Calvert, A. Morrin, G.G. Wallace, S.E. Moulton, Electro-stimulated release from a reduced graphene oxide composite hydrogel, J. Mater. Chem. B 3 (2015) 2530–2537, https://doi.org/10.1039/c5tb00050e.
[61] J. Song, B. Sun, S. Liu, W. Chen, Y. Zhang, C. Wang, X. Mo, J. Che, Y. Ouyang, W. Yuan, C. Fan, Polymerizing pyrrole coated poly (l-lactic acid-co-ε-caprolactone) (PLCL) conductive nanofibrous conduit combined with electric stimulation for long-range peripheral nerve regeneration, Front. Mol. Neurosci. 9 (2016) 117, https://doi.org/10.3389/fnmol.2016.00117.
[62] L.P. da Silva, S.C. Kundu, R.L. Reis, V.M. Correlo, Electric phenomenon: a disregarded tool in tissue engineering and regenerative medicine, Trends Biotechnol. 38 (2020) 24–49, https://doi.org/10.1016/j.tibtech.2019.07.002.
[63] C. Yu, F. Yao, J. Li, Rational design of injectable conducting polymer-based hydrogels for tissue engineering, Acta Biomater. 139 (2022) 4–21, https://doi.org/10.1016/j.actbio.2021.04.027.
[64] J. Venkatesan, I. Bhatnagar, P. Manivasagan, K.H. Kang, S.K. Kim, Alginate composites for bone tissue engineering: a review, Int. J. Biol. Macromol. 72 (2015) 269–281, https://doi.org/10.1016/j.ijbiomac.2014.07.008.
[65] M. Farokhi, F. Jonidi Shariatzadeh, A. Solouk, H. Mirzadeh, Alginate based scaffolds for cartilage tissue engineering: a review, Int. J. Polym. Mater. Polym. Biomater. 69 (2020) 230–247, https://doi.org/10.1080/00914037.2018.1562924.
[66] N. Siddiqui, S. Asawa, B. Birru, R. Baadhe, S. Rao, PCL-based composite scaffold matrices for tissue engineering applications, Mol. Biotechnol. 60 (2018) 506–532, https://doi.org/10.1007/s12033-018-0084-5.
[67] V. Gies, G. Lopinski, J. Augustine, T. Cheung, O. Kodra, S. Zou, The impact of processing on the cytotoxicity of graphene oxide, Nanoscale Adv. 1 (2019) 817–826, https://doi.org/10.1039/c8na00178b.
[68] E. Díaz, N. Iglesias, S. Ribeiro, S. Lanceros-Méndez, Cytocompatible scaffolds of poly(L-lactide)/reduced graphene oxide for tissue engineering, J. Biomater. Sci. Polym. Ed. 32 (2021) 1406–1419, https://doi.org/10.1080/09205063.2021.1922023.
[69] S. Chakraborty, T. Ponrasu, S. Chandel, M. Dixit, V. Muthuvijayan, Reduced graphene oxide-loaded nanocomposite scaffolds for enhancing angiogenesis in tissue engineering applications, R. Soc. Open Sci. 5 (2018), https://doi.org/10.1098/rsos.172017.
[70] S. Mukherjee, P. Sriram, A.K. Barui, S.K. Nethi, V. Veeriah, S. Chatterjee, K. I. Suresh, C.R. Patra, Graphene oxides show angiogenic properties, Adv. Healthc. Mater. 4 (2015) 1722–1732, https://doi.org/10.1002/adhm.201500155.

[71] K.Y. Lee, D.J. Mooney, Alginate: properties and biomedical applications, Prog. Polym. Sci. 37 (2012) 106–126, https://doi.org/10.1016/j.progpolymsci.2011.06.003.
[72] H. Mnatsakanyan, P. Rico, E. Grigoriou, A. Maturana Candelas, A. Rodrigo-Navarro, M. Salmeron-Sanchez, R. Sabater, I. Serra, Controlled assembly of fibronectin nanofibrils triggered by random copolymer chemistry, ACS Appl. Mater. Interfaces 7 (2015) 18125–18135, https://doi.org/10.1021/acsami.5b05466.
[73] D.R. Sahoo, T. Biswal, Alginate and its application to tissue engineering, SN Appl. Sci. 3 (2021) 1–19, https://doi.org/10.1007/s42452-020-04096-w.
[74] P.B. van Wachem, T. Beugeling, J. Feijen, A. Bantjes, J.P. Detmers, W.G. van Aken, Interaction of cultured human endothelial cells with polymeric surfaces of different wettabilities, Biomaterials 6 (1985) 403–408, https://doi.org/10.1016/0142-9612(85)90101-2.
[75] E. Ngandu Mpoyi, M. Cantini, P.M. Reynolds, N. Gadegaard, M.J. Dalby, M. Salmerón-Sánchez, Protein adsorption as a key mediator in the nanotopographical control of cell behavior, ACS Nano 10 (2016) 6638–6647, https://doi.org/10.1021/acsnano.6b01649.
[76] X.J. Loh, P. Peh, S. Liao, C. Sng, J. Li, Controlled drug release from biodegradable thermoresponsive physical hydrogel nanofibers, J. Control. Release 143 (2010) 175–182, https://doi.org/10.1016/j.jconrel.2009.12.030.
[77] Y. Wang, Y. Xiao, G. Gao, J. Chen, R. Hou, Q. Wang, L. Liu, J. Fu, Conductive graphene oxide hydrogels reduced and bridged by l-cysteine to support cell adhesion and growth, J. Mater. Chem. B 5 (2017) 511–516, https://doi.org/10.1039/c6tb02333a.
[78] L. Jin, D. Wu, S. Kuddannaya, Y. Zhang, Z. Wang, Fabrication, characterization, and biocompatibility of polymer cored reduced graphene oxide nanofibers, ACS Appl. Mater. Interfaces 8 (2016) 5170–5177, https://doi.org/10.1021/acsami.6b00243.
[79] S.R. Shin, C. Zihlmann, M. Akbari, P. Assawes, L. Cheung, K. Zhang, V. Manoharan, Y.S. Zhang, M. Yüksekkaya, K.T. Wan, M. Nikkhah, M.R. Dokmeci, X.S. Tang, A. Khademhosseini, Reduced graphene oxide-GelMA hybrid hydrogels as scaffolds for cardiac tissue engineering, Small 12 (2016) 3677–3689, https://doi.org/10.1002/smll.201600178.
[80] X. Shi, H. Chang, S. Chen, C. Lai, A. Khademhosseini, H. Wu, Regulating cellular behavior on few-layer reduced graphene oxide films with well-controlled reduction states, Adv. Funct. Mater. 22 (2012) 751–759, https://doi.org/10.1002/adfm.201102305.
[81] A. Star, Y. Liu, K. Grant, L. Ridvan, J.F. Stoddart, D.W. Steuerman, M.R. Diehl, A. Boukai, J.R. Heath, Noncovalent side-wall functionalization of single-walled carbon nanotubes, Macromolecules 36 (2003) 553–560, https://doi.org/10.1021/ma021417n.
[82] R. Ayala, C. Zhang, D. Yang, Y. Hwang, A. Aung, S.S. Shroff, F.T. Arce, R. Lal, G. Arya, S. Varghese, Engineering the cell-material interface for controlling stem cell adhesion, migration, and differentiation, Biomaterials 32 (2011) 3700–3711, https://doi.org/10.1016/j.biomaterials.2011.02.004.
[83] B. Guo, P.X. Ma, Conducting polymers for tissue engineering, Biomacromolecules 19 (2018) 1764–1782, https://doi.org/10.1021/acs.biomac.8b00276.
[84] H.S. Yang, B. Lee, J.H. Tsui, J. Macadangdang, S.Y. Jang, S.G. Im, D.H. Kim, Electroconductive nanopatterned substrates for enhanced myogenic differentiation and maturation, Adv. Healthc. Mater. 5 (2016) 137–145, https://doi.org/10.1002/adhm.201500003.